

Research Article

Experimental and Numerical Investigation into Formation of Metro Wheel Polygonalization

Wubin Cai ¹, Maoru Chi ¹, Gongquan Tao,¹ Xingwen Wu ², and Zefeng Wen ¹

¹State Key Laboratory of Traction Power, Southwest Jiaotong University, Chengdu 611031, China

²School of Mechanical Engineering, Southwest Jiaotong University, Chengdu 611031, China

Correspondence should be addressed to Maoru Chi; cmr2000@163.com

Received 3 March 2019; Revised 13 May 2019; Accepted 13 June 2019; Published 1 July 2019

Academic Editor: Jörg Wallaschek

Copyright © 2019 Wubin Cai et al. This is an open access article distributed under the Creative Commons Attribution License, which permits unrestricted use, distribution, and reproduction in any medium, provided the original work is properly cited.

We present a detailed investigation of the mechanism of metro wheel polygonal wear using on-site experiments and numerical simulation. More than 70% of metro wheels exhibit 6th–8th harmonic-order polygonal wear; the excitation frequency of the polygonal wear is located in the 50–70 Hz interval at an operating speed of 65–75 km/h. To determine the root cause of the polygonal wear, a dynamic train behavior test is conducted immediately after wheel reprofiling. The results suggest a natural mode resonance in the vehicle/track system, whose frequency coincides with the passing frequency of the 6th–8th order polygonalization. The magnitude of the resonance increases significantly when the vehicle runs on a monolithic concrete bed with DTVI2 fasteners. Thus, a corresponding coupled vehicle/track dynamic model is established and validated by comparing the calculated frequency response functions (FRFs) of tracks and dynamic responses of axlebox acceleration with the measured values. Using multiple timescales, the dynamic model and Archard wear model are integrated in a closed loop for long-term polygonal wear prediction. The simulated and measured evolution of polygonal wear show good agreement. By combining simulation results and experimental data, we suggest that the P2 resonance is the main contributor to the high amplitude of wheel/rail contact forces in the 50–70 Hz frequency range and the reason for subsequent polygonal wear. Parametric studies show that the dominant order decreases as vehicle speeds increase, representing a “frequency-constant” mechanism. The wheelset flexibility, especially the bending mode, would aggravate the wheel/rail creepage and further accelerate the formation of polygonal wear. Higher rail pad stiffness will increase P2 resonance frequency and shift the dominant wheel to higher polygonal orders.

1. Introduction

Wheel polygonalization, also known as wheel corrugation or periodic out-of-round (OOR) wheels, is one of the greatest concerns in railway vehicles and is defined as periodic radial tread irregularity around the circumference superimposed on a constant wheel radius [1]. According to previous investigations, wheel polygonalization is a global phenomenon in different types of the railway vehicle. Polygonalization in the first, third, and fourth orders was measured by Zacher [2] on wheels of ICE trains in Germany. Pallgen [3] made a contrasting analysis on the wavelength of wheel polygonalization in different types of ICE train wheels; they found that the third order was the dominant order on solid steel wheels, while the second order dominated for rubber sprung wheels. Rode [4] stated

that fixation during the wheel reprofiling process may lead to the initial third-order out-of-round wheels. Kaper [5] described the polygonalization phenomenon on the Netherlands railway and indicated that hot spots and hardening effects between the cast-iron brake block and wheel tread during braking is the main contributor to polygonalization. Similar results were also observed by Dings [6] after measuring more than 140 wheels on the Netherlands Intercity trains with different braking systems. They found that wheels with discs and additional cast-iron block brakes had the highest roughness levels in polygonal wear with wavelengths at intervals of 5–7 cm. The effect of thermomechanical interaction between the brake block and wheel tread on wheel corrugation was further investigated by Vernersson [7, 8] through both experimental and numerical methods.

An overview of wheel polygonalization in Sweden was given by Johansson [9], whose results suggested that most wheels on freight train and powered high-speed train wheels had high eccentricity levels and high roughness for wavelengths from 30 to 80 mm. In North America, Snyder [10] studied wheel polygonalization on a full-scale test rig. The author noted that wheel spalling and wheel eccentricity may be causative factors of polygonal wear. In recent years, the Chinese railway has also suffered from serious wheel polygonalization. Jin [11] carried out a detailed investigation into the mechanisms behind ninth-order polygonal wear in LIM metro trains. Their experiments showed that the first bending mode of the wheelset was excited during operation, which led to oscillation of the wheel/rail normal forces, lateral creepage, and further periodic variations of material wear. After a long period of service, ninth-order wheel polygonal wear gradually formed. Tao [12] reported polygonal wear measurements on more than 2000 wheels of seven different types of locomotive used in China; 18th, 19th, and 24th order polygonalization dominated for wheels on two types of freight traffic locomotive. Further experimental investigation [13] suggested that wheelset first bending resonance may be the root cause of 18th-19th order polygonalization, while 24th order polygonalization may be attributed to lateral bending resonance of the wheel disc. High-order wheel polygonal wear was observed on Chinese high-speed EMU train wheels; at operating speeds of 300 km/h, the wheel exhibited 18th-20th order polygonalization [14-18], while 23rd-24th order wheel polygonalization dominated under operating speeds of 250 km/h [19]. However, the passing frequency of a different polygonalization in Chinese high-speed trains displays almost the same interval (approximately 550-600 Hz). Therefore, it is assumed that the so-called "constant-frequency" mechanism in the vehicle/track system initiates high-order wheel polygonalization. Unfortunately, the exact origin of this "constant-frequency" vibration has remained in dispute until now.

The effect of wheel polygonalization on the dynamic response of the vehicle and track system has been widely investigated both theoretically and experimentally [16, 17, 19-23]. Liu [20] reported that periodic polygonal wheels cause considerable dynamic loads in a wide speed range, while for stochastic polygonal wheels, rail/wheel contact forces become more sensitive at higher train speeds. Using a flexible wheelset model, Mazilu [22] found that wheel/rail contact forces increase when the passing frequency of the OOR interacts with the bending mode of the wheelset; similar results were obtained by Han [23]. Wu [16] investigated the dynamic response of a high-speed vehicle under 18th order polygonal wear. The results suggested that high-order polygonalization leads to extreme acceleration on the axlebox and wheel/rail normal forces at high speeds and even wheel/rail separation at relatively low speeds when resonance occurs. Wang [24] described the evolution of axlebox vibration signals versus the high-order polygonalization growth process in long-term field tests, revealing that high-order polygonalization can form in a short time once wheels experience sudden damages, such as flats.

Through extensive experiments and numerical simulation, Zhang [18] evaluated the effect of OOR on the noise of

high-speed trains and reported that wheel polygons of higher order lead to more serious wheel/rail and interior noise. Apart from inducing wheel/rail impact forces and noise, wheel polygonalization will also reduce the fatigue life of vehicles and track components. The derailment of an ICE train in 1998 was attributed to a fatigue crack in the wheel rim caused by a nonround wheel [1]. Through a modal stress recovery method, Wu [14] showed that the dynamic stress of a wheelset axle will increase considerably when wheel polygonal wear excites the resonance of the wheelset axle. The author also performed a damage tolerance analysis in the presence of wheel polygonalization [15], which indicated that polygonalization-induced impact can reduce the residual lifetime of the wheelset axle. In most cases, railway operators should reduce the intervals between inspections and wheel reprofiling to guarantee the reliability of vehicle and track components; however, this is not an economic approach.

In order to prevent or slow the growth of wheel polygonalization, it is necessary to understand the formation mechanism of polygonalization. Many mathematical models have been proposed to predict the growth of polygonal wear. One basic assumption is the multiple timescale [25, 26], whereby a fast-time dynamic model to calculate forces and creepage at the wheel/rail interface and a slow-time wear model to determine the material excavation are coupled in a long-term polygonal wear iterative process. Morys [27] investigated the enlargement process of an initial ideal OOR with 1-5th order polygonalization. The results suggested that the original wheel OOR will exhibit large normal force variations and excite the bending oscillation of the wheelset, which will further lead to lateral slip and lateral material excavation between the wheel and rail. In addition, track properties play an important role in the wear progress of OOR. According to the flexibility of the wheelset, Meinke and Meinke [28] studied wheel polygonalization in modern high-speed trains due to wheel imbalance. Their numerical results showed that polygonalization will grow to unacceptable values in the presence of dynamic imbalance, even with a perfectly round initial wheel. In research by Meymerk [29], in which a change in the wear rate was considered in each wear iteration, it was found that the first and second bending modes of the wheelsets could be critical contributors to wheel polygonalization. Moreover, comparing OOR of the same phase, a large phase shift in the OOR between the left and right wheels of the same axle may in turn accelerate OOR growth. A detailed coupled vehicle/track model validated by experimental data was established by Johansson and Andersson [25], who used it to investigate the development of OOR based on an initial irregularity spectrum derived from measurements conducted on new wheels. The simulation suggested that vertical track antiresonance and P2 resonance will increase OOR amplitudes of corresponding orders.

This study presents a detailed investigation of the mechanism of wheel polygonalization on a metro line in China through both extensive experiments and numerical simulation. In the experimental section, we measure the polygonal wear of 188 wheels and obtain the dynamic behavior of the vehicle during operation. For a better understanding of polygonal wear formation, a long-term

polygonal wear iteration model is then developed, composed of a comprehensive coupled vehicle/track dynamic model and an Archard wear model. In the dynamic model, the track system is treated as two Timoshenko beams discretely resting on the slabs via fasteners; the slab is described by the finite-element method. The validity of the model is demonstrated by comparing the track frequency response functions (FRFs) and acceleration of the axlebox to the field-measured data. Then, the evolution of polygonalization, beginning from measured new wheel irregularity, is simulated with different parameters using the long-term wear iteration model. Consequently, by combining the experimental and simulation results, we identify the root causes of the polygonalization.

2. Wheel Polygonalization Experiments

2.1. Measurement of Wheel Polygonalization. Recently, the trains of one metro line in China suffered wheel polygonalization; thus, the polygonal wear of 188 wheels on 4 trains operating on that line are measured using a Müller-BBM wheel roughness measurement device, as shown in Figure 1. The operating mileage after the last reprofiling of these trains ranges from 70,000 to 150,000 km. From the statistical results, it is found that 6–8th order polygonal wear dominates in more than 70% of all measured wheels. Figure 2 shows four types of typical wheel polygonalization described in the polar coordinate system and an order graph. Tao [12] presented a detailed measurement procedure and wheel irregularity analysis method. The wheel roughness (dB re 1 μm) is calculated using the discrete Fourier transform and defined as follows:

$$L_k = 10 \log_{10} \left(\frac{S}{S_{\text{ref}}} \right), \quad (1)$$

where S is the roughness obtained through the narrow band spectrum of wheel irregularities and $S_{\text{ref}} = 1 \mu\text{m}$. As it is shown in Figure 2, the wheel wear exhibits a combination of several different orders, while the wheel eccentricity (1st order) and polygonal wear of the 6–8th order have the highest roughness level. Such wheel polygonalization is unlike that previously observed on high-speed trains [14–19, 24] and electric locomotives [12, 13]; the latter are always characterized by a regular harmonic waveform with a constant wavelength along the wheel circumference. This is probably because high-speed trains and electric locomotives in China tend to maintain a constant operating speed over long-distance operation, while the metro's operational speed varies frequently due to the short station intervals. This variation of speeds disturbs the wavelength of wheel polygonal wear from a "frequency-constant" mechanism [30]. The distribution of the test metro train's speed is illustrated in Figure 3. The common operation speed is in the range of 60–75 km/h, which accounts for more than 65% of total operation. The diameter of the wheels is around 840 mm; therefore, the wavelength of 6–8th polygonal wear is 330–430 mm and the excitation frequency is given by the following equation:

$$f_{\text{oor}} = \frac{V}{D\pi/N} = \frac{(65 \sim 75)/3.6}{0.84\pi/(6 \sim 8)} = 41 \sim 63 \text{ Hz}. \quad (2)$$



FIGURE 1: Wheel polygonalization measurements in field tests.

2.2. Measurement of Axlebox Vertical Accelerations. The vehicle/track system is under forced vibration conditions once wheel polygonalization has formed. Therefore, in order to understand the initial formation stage of wheel polygonalization, the accelerations of the vehicle are measured immediately after wheel reprofiling. Wheel irregularity along the circumference of the tested vehicle after reprofiling is presented in Figure 4, and the 6–8th order wheel polygonalization is removed. Furthermore, the roughness of the track irregularity is measured; corrugation with relevant wavelengths at 330–430 mm is not found. Under these circumstances, we can assume that the vehicle/track system is only subjected to stochastic irregularities. There are four main types of the track structure in the studied metro line: monolithic concrete bed with DTVI2 fasteners (large vertical stiffness), monolithic concrete bed with compression-type fasteners (small vertical stiffness), low-weight floating slab track, and high-weight floating slab track. The lengths of these four track types account for 54%, 25%, 9%, and 10% of the total line length, respectively. The accelerometers are arranged on the axlebox when the test train operates, the sampling frequency of the accelerometer on the axlebox is up to 8192 Hz, and Figure 5(a) shows the vertical accelerations of the axlebox when the vehicle traverses the section containing all four types of the track structure, as well as the vehicle speed curve. The axlebox shows different vibrational amplitudes in different track structures. To further identify the vibration characteristics in the time-frequency domain, short time Fourier transform (STFT) is performed, the analysis frequency is 0–200 Hz, and its resolution is 0.2 Hz. In Figure 5(b), the horizontal and vertical axes represent time and frequency, respectively, and the amplitude of acceleration is denoted by the color depth. As it can be seen, a bright band in the range of 50–70 Hz is observed in the whole operation section regardless of the vehicle speed. However, the frequency characteristics of the axlebox vibration on different tracks show some differences. In Figure 6, the axlebox acceleration when the vehicle is running at 60–75 km/h on different tracks is converted to the frequency domain, respectively; ten-second data are selected for each type of track. It is found that the dominant frequencies of the vertical acceleration of axlebox are at around 63 Hz, 48 Hz, 68 Hz, and 68 Hz corresponding to these four types of tracks. Especially, when running on the monolithic concrete bed with DTVI2 fasteners, the dominant frequency

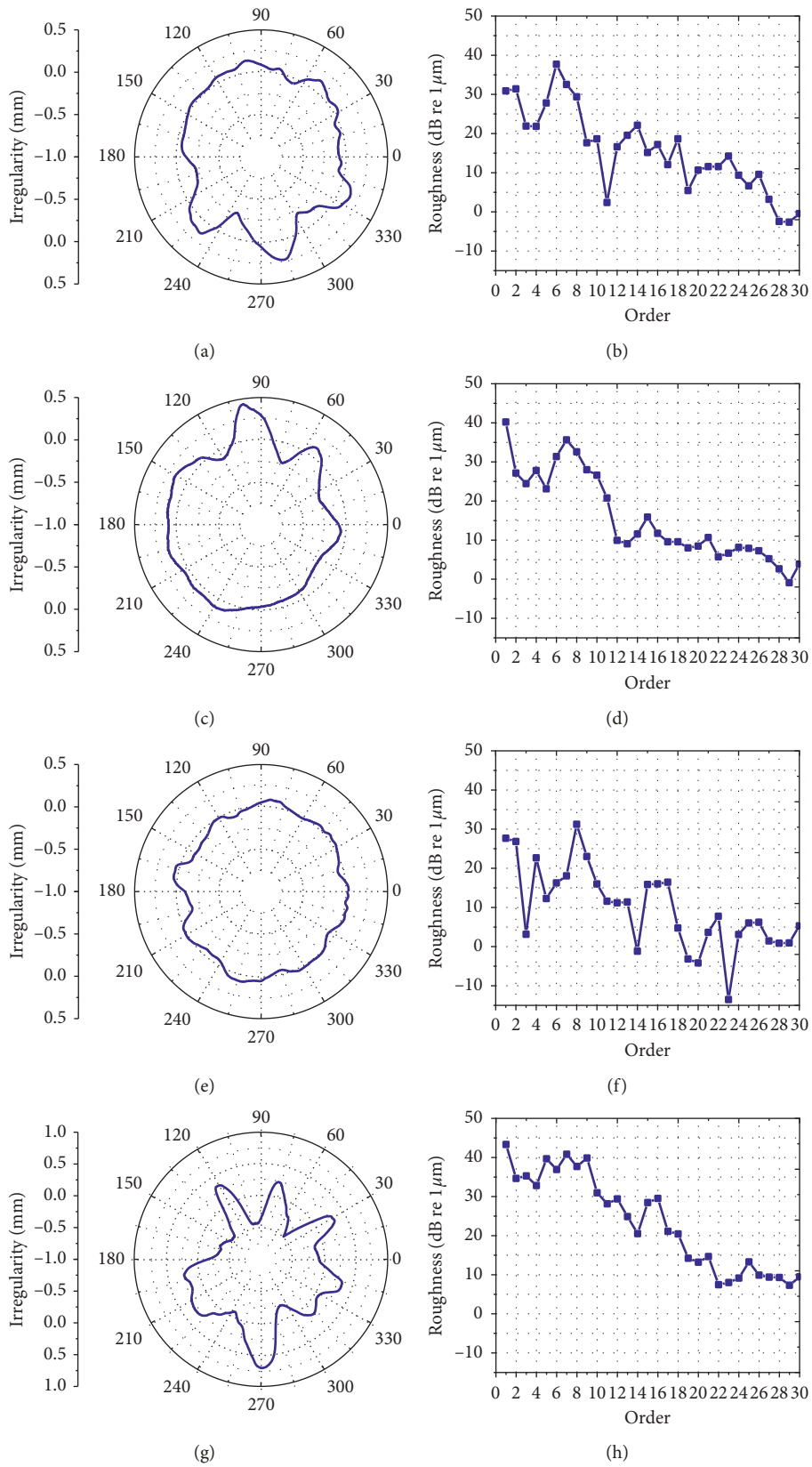


FIGURE 2: Typical types of wheel polygonalization measured on metro wheels.

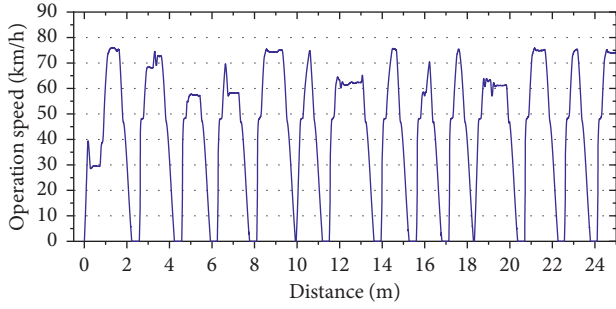


FIGURE 3: Distribution of metro train operation speeds.

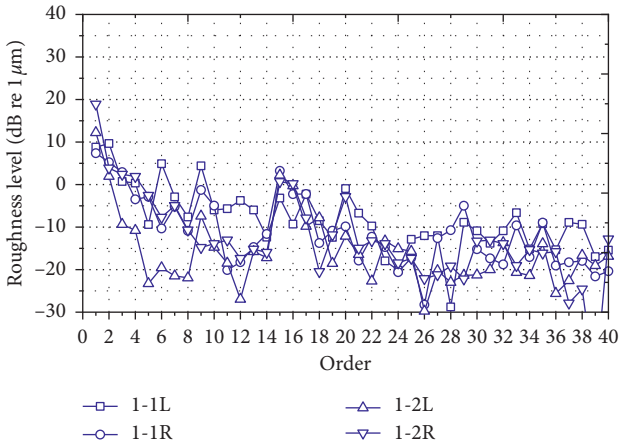


FIGURE 4: Spatial spectrum of wheel irregularity obtained on the test vehicle after reprofiling.

is more concentrated and its peak value is higher than three other tracks.

In summary, the dominant frequency of the axlebox acceleration right after the wheel reprofiling is coincident with the excitation frequency of 6–8th order polygonalization. And the frequency is independent of vehicle speed, which indicates that this vibration is related to the natural characteristics of the vehicle/track system. We therefore deduce that natural resonance at a frequency of 50–70 Hz in the vehicle/track system is the driving factor for formation of wheel polygonalization. In the following section, we identify the origin of this resonance.

3. Long-Term Wear Iteration Model

A long-term wear iteration model is established in this section to predict the formation of metro wheel polygonalization. This model includes two parts: a model of coupled vehicle/track dynamics to calculate the dynamic response at the wheel/rail interface and a wear model to evaluate the wear depth along the wheel circumference. In the simulation scheme, the dynamic model and the wear model are integrated in a closed loop, extending to the polygonalization wear prediction model on the basis of multiple timescales.

3.1. Coupled Vehicle/Track Dynamic Model. The coupled vehicle/track dynamic model is formulated using a slab track

model and a vehicle multibody model. In order to cover the excitation frequency of polygonalization, the track system is treated as flexible by the modal synthesis method.

3.1.1. Track Subsystem. Although there are three types of slabs, the proportion of the monolithic concrete bed track is more than 78% of the metro line, and the experimental results suggest that the axlebox vibration with a frequency of 50–70 Hz has the largest amplitude on the monolithic concrete bed track with DTVI2 fasteners. Therefore, the monolithic concrete bed track is evaluated in this study. As Figure 7 shows, the track system is modeled as two continuous rail beams discretely supported on the monolithic concrete bed using the fasteners. The rail and the monolithic concrete bed are formulated by the Timoshenko beam theory and finite-element method, respectively, while the fasteners and flexible foundation supports are treated as a set of spring-damper elements. Vertical, lateral, and torsion deformation of the rail are taken into consideration.

On the basis of the Timoshenko beam theory and modal superposition method, the deflection of the rail can be expressed as a set of second-order ordinary differential equations [31]:

$$\ddot{q}_{yk}(t) + \frac{\kappa_y GA}{\rho A} \left(\frac{k\pi}{l} \right)^2 q_{yk}(t) - \kappa_y GA \frac{k\pi}{l} \sqrt{\frac{1}{\rho^2 AI_z}} \omega_{yk}(t)$$

$$= - \sum_{i=1}^{N_s} F_{syi} Y_k(x_{si}) + \sum_{j=1}^{N_w} F_{wryj} Y_k(x_{wj}),$$

$$\ddot{\omega}_{yk}(t) + \left[\frac{\kappa_y GA}{\rho I_z} + \frac{EI_z}{\rho I_z} \left(\frac{k\pi}{l} \right)^2 \right] \omega_{yk}(t)$$

$$- \kappa_y GA \frac{k\pi}{l} \sqrt{\frac{1}{m\rho I_z}} q_{yk}(t) = 0,$$

$$\ddot{q}_{zk}(t) + \frac{\kappa_z GA}{\rho A} \left(\frac{k\pi}{l} \right)^2 q_{zk}(t) - \kappa_z GA \frac{k\pi}{l} \sqrt{\frac{1}{\rho^2 AI_y}} \omega_{zk}(t)$$

$$= - \sum_{i=1}^{N_s} F_{szi} Z_k(x_{si}) + \sum_{j=1}^{N_w} F_{wrzj} Z_k(x_{wj}),$$

$$\ddot{\omega}_{zk}(t) + \left[\frac{\kappa_z GA}{\rho I_y} + \frac{EI_y}{\rho I_y} \left(\frac{k\pi}{l} \right)^2 \right] \omega_{zk}(t)$$

$$- \kappa_z GA \frac{k\pi}{l} \sqrt{\frac{1}{\rho^2 AI_y}} q_{zk}(t) = 0,$$

$$\ddot{q}_{Tk}(t) + \frac{GK}{\rho I_0} \left(\frac{k\pi}{l} \right)^2 q_{Tk}(t) = - \sum_{i=1}^{N_s} M_{si} \Phi_k(x_{si})$$

$$+ \sum_{j=1}^{N_w} M_{Gj} \Phi_k(x_{wj}).$$

(3)

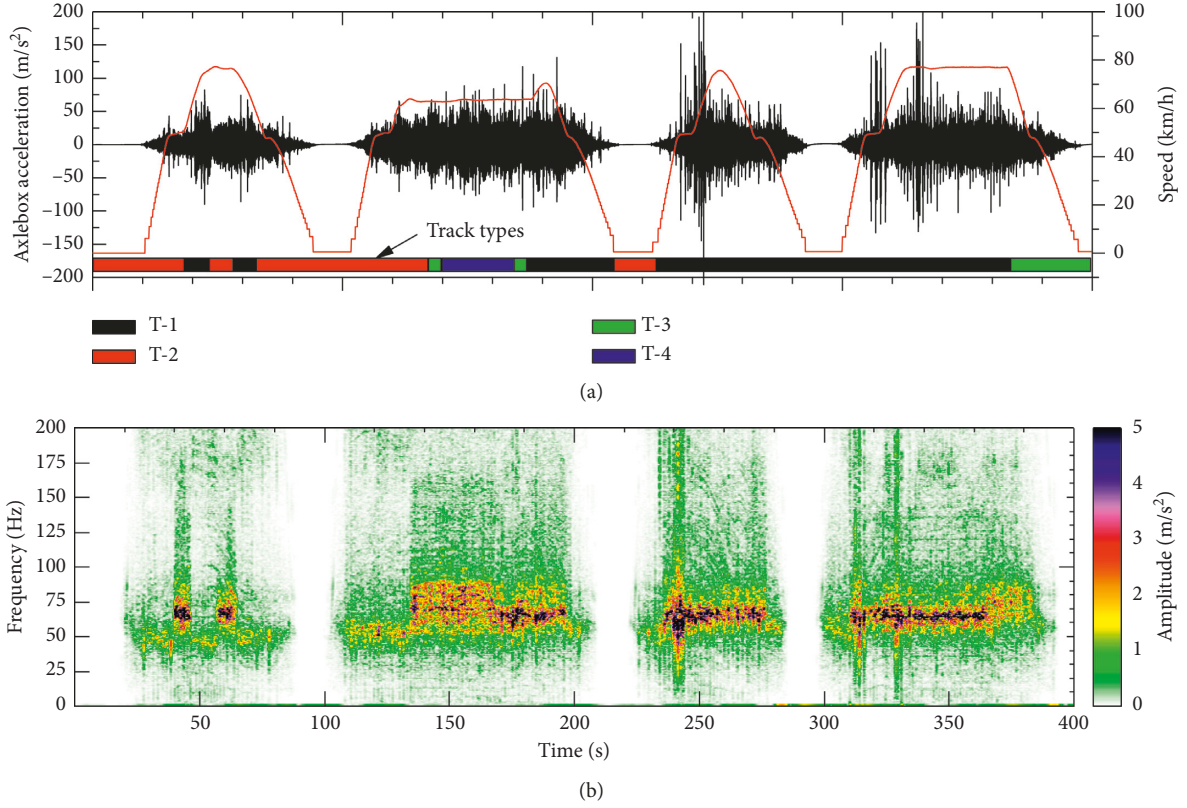


FIGURE 5: Measured vertical acceleration of the axlebox right after wheel reprofiling: (a) time-domain signal for a vehicle running on different types of track (T-1 for monolithic concrete bed with DTVI2 fasteners, T-2 for monolithic concrete bed with compression-type fasteners, T-3 for low-weight floating slab track, and T-4 for high-weight floating slab track); (b) time-frequency spectra of acceleration.

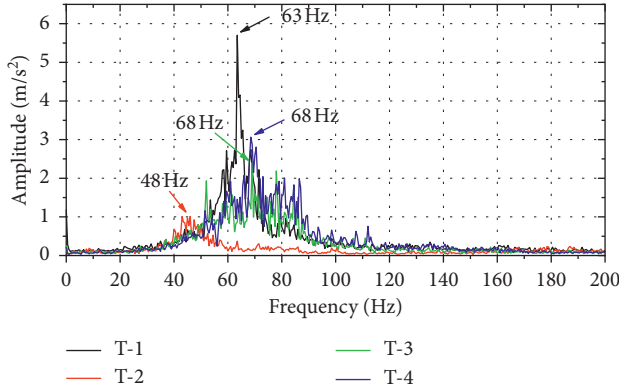


FIGURE 6: Frequency spectral of the vertical axlebox accelerations on different types of tracks (T-1 for monolithic concrete bed with DTVI2 fasteners, T-2 for monolithic concrete bed with compression-type fasteners, T-3 for low-weight floating slab track, and T-4 for floating slab track with high weight).

where q_{yk} , q_{zk} , and q_{Tk} are the generalized coordinates of lateral, vertical, and torsional deflection of rail; ω_{yk} and ω_{zk} are the generalized coordinates for the cross-sectional rotation of rail; F_{wryj} , F_{wrzj} , and M_{Gj} are the moving wheel/rail contact forces and moment owing to the j^{th} wheel; F_{syi} , F_{szi} , and M_{sj} are the support forces due to the i^{th} rail pad; E and G are Young's modulus and the shear modulus for the rail material; ρ represents the rail

density; A is the area of rail cross section; EI_y , EI_z , and GK are the vertical bending, lateral bending, and torsional stiffness of the rail; κ_y and κ_z are the lateral and vertical shear coefficient of the rail; x_{si} and x_{wj} denote the longitudinal position of the fasteners and wheels along the rails; and N_s and N_w are the total numbers of the fasteners and wheels in the model.

According to the modal superposition principle of beams, the lateral, vertical, and torsional deflection of rail y , z , and ϕ can be written as the linear superposition of modal shapes:

$$\begin{aligned}
 y(x, t) &= \sum_{k=1}^{NL} Y_k(x) q_{yk}(t), \\
 z(x, t) &= \sum_{k=1}^{NV} Z_k(x) q_{zk}(t), \\
 \phi(x, t) &= \sum_{k=1}^{NT} \Phi_k(x) q_{Tk}(t),
 \end{aligned} \tag{4}$$

where $Y_k(x)$, $Z_k(x)$, and $\Phi_k(x)$ are the mode shape function of simply supported beam. NL , NV , and NT denote the cut-off modal numbers in the calculation; in this study, 250 modes of the rail in each direction are taken into consideration.

As it is not easy to describe the slab using analytic methods, the finite-element method is adopted to discretize the monolithic concrete bed (Figure 8). In global

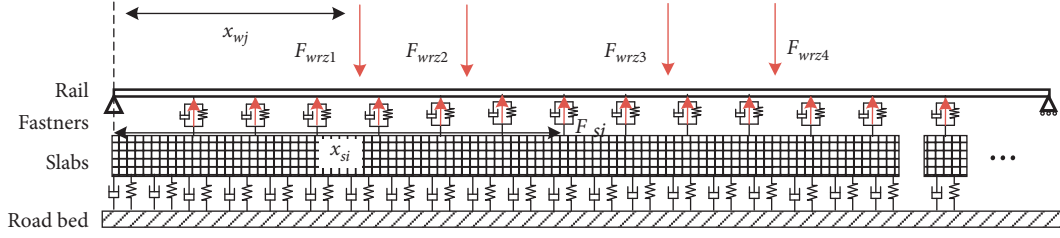


FIGURE 7: Monolithic concrete bed track model.

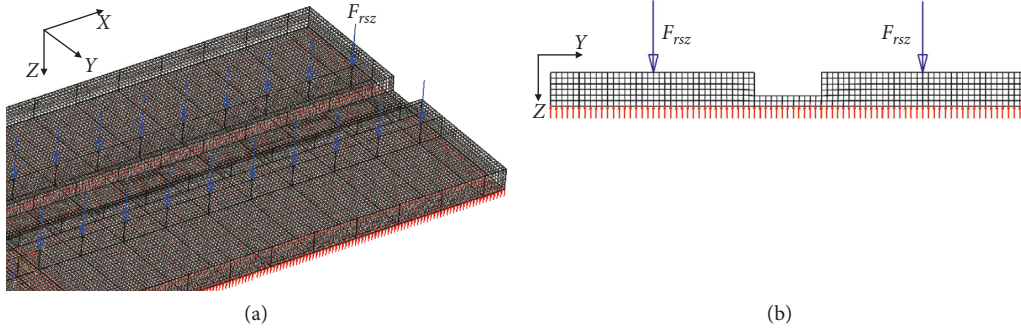


FIGURE 8: Finite-element model for a monolithic concrete bed.

coordinates, the equations of motion for a single monolithic concrete bed can be expressed as follows:

$$[M]\{\ddot{x}\} + [C]\{\dot{x}\} + [K]\{x\} = \{F_{rs}\} + \{F_g\}, \quad (5)$$

where $[M]$, $[C]$, and $[K]$ are the mass matrix, damping matrix, and stiffness matrix, respectively; $\{F_{rs}\}$ denotes the interaction forces between the slab and rail; and $\{F_g\}$ refers to the foundation support forces. Using the modal superposition principle [32], Equation (5) is transformed into a set of uncoupled equations:

$$\begin{aligned} \ddot{X}_{ni} + 2\zeta_n\omega_n\dot{X}_{ni} + \omega_n^2X_{nk} &= \{\phi\}_n^T \{F_k^{rs}\} + \{\phi\}_n^T \{F_k^g\}, \\ (n = 1 \sim N_{\text{mode}})(k = 1 \sim N_{\text{slab}}), \end{aligned} \quad (6)$$

in which X_{nk} represents the generalized modal coordinates of the slab k and $\{\phi\}_n$ and ω_n are the modal shape vector and natural frequency for mode n . The displacement of the slab can be described by superposition of the modal shapes:

$$x = \sum_{i=1}^{N_{\text{mode}}} \{\phi\}_n X_n. \quad (7)$$

In this study, the modal shape vectors and their corresponding natural frequencies of the slab are calculated by the modal analysis in the ANSYS platform.

Validation of the track model is performed by comparing the calculated FRFs to the on-site measurement results. In the simulation, the acceleration response is first obtained in the time domain when applying a sinusoidal force at the railhead. The FRFs are then determined through the acceleration amplitude divided by the force amplitude; the frequency of the sinusoidal force is

10–1500 Hz. In experiments, the track FRFs are achieved by the hammer-impact excitation method; the vertical FRFs of the railhead at the midspan between two sleepers and above the sleeper are both tested. From Figure 9(a), two resonance can be identified when the excitation point is at the midspan. The first resonance is at approximately 204 Hz; here, the rail presents a large bending vibration relative to the slab. The peak at 1110 Hz is the so-called pinned-pinned rail resonance, at which the half wavelength of the rail vibration fits well with the sleeper spacing. When the hammer impacts over the sleeper, the FRFs at the pinned-pinned frequency become a valley, as shown in Figure 9(b). The simulation results agree well with the measurements at low resonance although the calculated pinned-pinned frequency is a little higher than the measurements. This may be due to the fastener system treated as a point support in the simulation, which neglects the effect of support width. However, the focus of this study is low-order polygonalization of the metro train. Frequencies up to 1000 Hz are difficult to excite; thus, deviations in the high frequency range have a minimal influence on the simulation of focused wheel polygonalization formation.

3.1.2. Vehicle Subsystem. Figure 10 illustrates the dynamic model of the metro vehicle. The vehicle is treated as a car body seated on two bogies through secondary suspension. Each bogie consists of two wheelsets and a bogie frame; the wheelsets are coupled to the bogie frame via first suspension. Each component has six rigid body degrees of freedom (DoF), including three translation motions and three rotation motions with respect to vertical, lateral, and

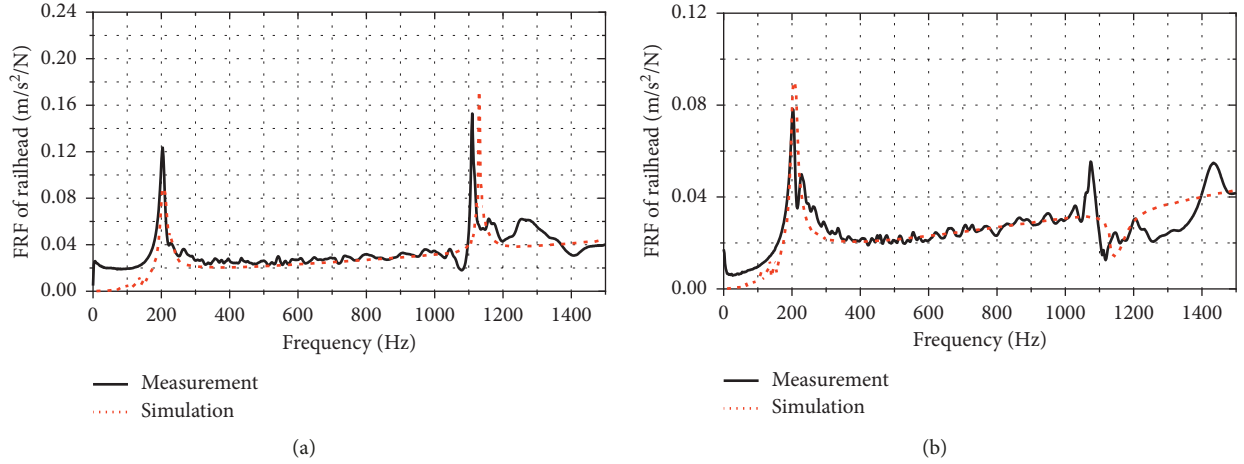


FIGURE 9: Comparison of measured and calculated vertical FRFs of the track system: (a) FRFs of the railhead at the midspan between two sleepers; (b) FRFs of the railhead over the sleeper.

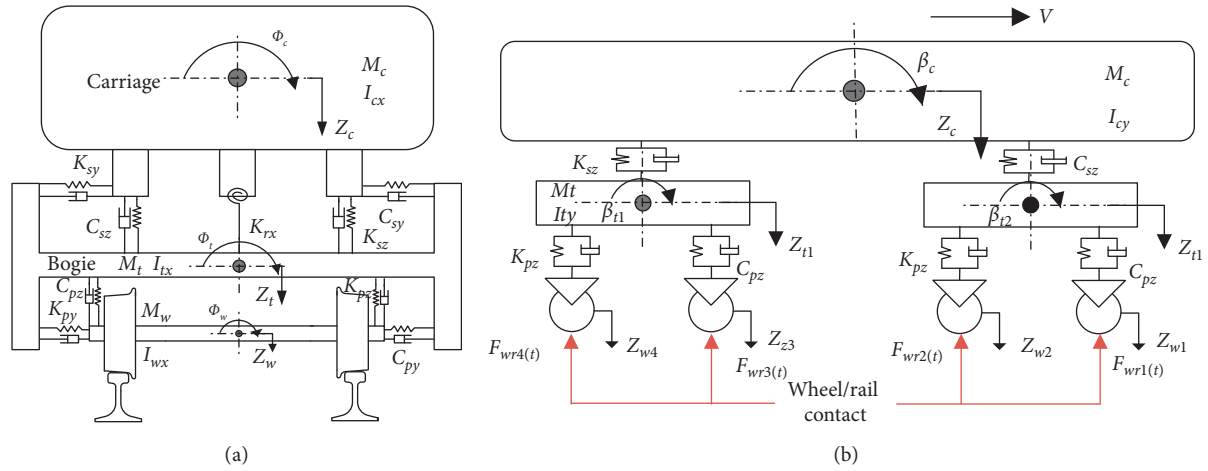


FIGURE 10: Schematic model of the vehicle: (a) front view; (b) side view.

longitudinal directions. The conventional motion equations of the vehicle can be found in [33]. The nominal parameters of the vehicle/track system are listed in Table 1. The dynamic equations are solved numerically using the Fortran codes.

3.2. Wear Model. Among many material wear hypotheses [34], the Archard model is widely used in the wheel/rail wear simulation due to its good accuracy [25, 35, 36], in which the volume of worn material V_{wear} is defined as follows:

$$V_{\text{wear}} = k_w \frac{Nd}{H}, \quad (8)$$

where k_w is the wear coefficient, whose value is dependent on the contact normal pressure and the slip velocity, H is the hardness of the softer material, N denotes the normal force, and d represents the sliding distance. In this study, the wavelength of the wheel polygonalization L we focused on is much larger than the radius of the contact patch R_c . According to Knothe's research [37], when $L/R_c > 10$, the stationary contact models are still thought valid. Thus, the Hertz contact theory and FASTSIM algorithm is adopted in

the wear calculation. The contact patch is divided into discrete elements according to FASTSIM, as shown in Figure 11(a).

The wear depth Δz in each element (x_{ij}, y_{ij}) at instant t^k follows the Archard model hypothesis:

$$\Delta z(x_{ij}, y_{ij}, t^k) = k_w \frac{p_z(x_{ij}, y_{ij}, t^k) \Delta d(x_{ij}, y_{ij}, t^k)}{H}, \quad (9)$$

where Δd is the elastic displacement during the one-time interval and can be expressed by multiplying the slip velocity with the time interval:

$$\begin{aligned} \Delta d(x_{ij}, y_{ij}, t^k) &= |s(x_{ij}, y_{ij}, t^k)| \Delta t \\ &= \sqrt{s_x(x_{ij}, y_{ij}, t^k)^2 + s_y(x_{ij}, y_{ij}, t^k)^2} \Delta x_j^k / v_c^k, \end{aligned} \quad (10)$$

in which Δx_j^k is the element length of strip j in the wheel forward direction, v_c^k is the speed of the material point moving through the contact patch, and s denotes the slip velocity, which can be obtained in the dynamic simulation:

TABLE 1: Parameter values of the track and vehicle subsystems.

Parameters	Value
<i>Track subsystem</i>	
Young's modulus of rail (N/m ²)	2.059×10^{11}
Shear modulus of rail (N/m ²)	7.9×10^{10}
Density of rail (N/m ²)	7860
Cross-sectional area (m ²)	7.745×10^{-3}
Bending moment about y-axis (m ⁴)	3.217×10^{-5}
Vertical shear coefficient	0.5329
Density of slab (kg/m ³)	2800
Young's modulus of slab (N/m ²)	3.6×10^{10}
Rail pad vertical stiffness (MN/m)	55
Rail pad vertical damping (kN·s/m)	10
Slab support vertical stiffness (MN/m)	2860
Slab support vertical damping (kN·s/m)	300
Sleeper spacing (m)	0.6
<i>Vehicle subsystem</i>	
Car body mass (kg)	36,632
Bogie mass (kg)	1800
Wheelset mass (kg)	1520
Car body pitch moment of inertia (kg·m ²)	1,184,990
Bogie pitch moment of inertia (kg·m ²)	1474
Secondary suspension vertical stiffness (MN/m)	0.45
Secondary suspension vertical damping (kN·s/m)	60
Primary suspension vertical stiffness (MN/m)	1.32
Primary suspension vertical damping (kN·s/m)	1.32
Wheel radius (m)	0.42
Half distance between two bogie frames (m)	6.3
Half of the bogie wheelbase (m)	1.1

$$s(x_{ij}, y_{ij}, t^k) = \begin{bmatrix} s_x(x_{ij}, y_{ij}, t^k) \\ s_y(x_{ij}, y_{ij}, t^k) \end{bmatrix} \quad (11)$$

$$= v_v^k \left(\begin{bmatrix} v_x^k - \phi^k y_{ij} \\ v_y^k - \phi^k x_{ij} \end{bmatrix} - \frac{\partial u(x_{ij}, y_{ij}, t^k)}{\partial x} \right),$$

where v_x^k , v_y^k , and ϕ^k are the creepages, u denotes the elastic displacements of the wheel relative to the rail, and v_v^k is the velocity of the vehicle and $v_v^k \approx v_c^k$. The Hertz contact theory is applied to evaluate the normal contact forces, and the normal pressure of each element can be determined by the following equation:

$$p_z(x_{ij}, y_{ij}, t^k) = \frac{3N}{2\pi a^k b^k} \sqrt{1 - \left(\frac{x_{ij}}{a^k}\right)^2 - \left(\frac{y_{ij}}{b^k}\right)^2}, \quad (12)$$

where a and b are the ellipse semiaxes of the contact patch. By substituting Equation (10) and Equation (12) into Equation (9), the wear depth in each element can be expressed as follows [25]:

$$\Delta z(x_{ij}, y_{ij}, t^k) = \frac{3Nk_w}{2\pi a^k b^k H} \sqrt{1 - \left(\frac{x_{ij}}{a^k}\right)^2 - \left(\frac{y_{ij}}{b^k}\right)^2} \cdot \sqrt{s_x(x_{ij}, y_{ij}, t^k)^2 + s_y(x_{ij}, y_{ij}, t^k)^2} \frac{\Delta x_j^k}{v_c^k}. \quad (13)$$

For each strip j at instant t^k , the wear can be expressed as the accumulation of elements' wear in the wheel rolling direction:

$$\Delta z_j^k = \sum_{i=1}^{nx} \Delta z(x_{ij}, y_{ij}). \quad (14)$$

In this study, only the circumferential wear is of interest. The wheel circumference is evenly divided into discrete points, as shown in Figure 11(b). The maximum wear depth of the strips in a contact patch $\Delta z^k = \max_{j=1}^{ny} (\Delta z_j^k)$ is taken as the wear depth of the wheel circumference points. Moreover, only the tangent track is considered, the wheel/rail sliding is relatively small, and the contact points are expected on the tread region. According to Jendel's measurements [38], under these circumstances, the wear is mild and the wear coefficient could be set to a small constant value $k_w = 1 \times 10^4$. And the hardness of the wheel tread is $H = 3.2$ GPa according to [25].

The LM wheel tread and CHN60 rail profile are considered in the wheel/rail contact model, which are widely used in China's medium- and low-speed trains. The geometric profiles of the LM tread and CHN60 are plotted in Figures 12(a) and 12(b). In order to eliminate the contact points jumping, the quasi-elastic contact algorithm [39] is applied to smooth the contact point distribution. The wheel/rail contact point pairs regarding different wheelset lateral displacements without the yaw angle are illustrated in Figure 12(c).

3.3. Long-Term Wear Iteration Scheme. Combined with the coupled vehicle/track dynamic model and wheel/rail wear model, a long-term wear prediction model is proposed [25, 26]. Figure 13 shows a flow chart of the main steps in polygonal wear prediction. At the beginning, initial wheel polygonal wear with a small amplitude (immediately after re-profiling) is attached to the circumference of each wheel. A short-term dynamic simulation is then carried out corresponding to 15 wheel revolutions, in which the first 5 wheel revolutions are eliminated to exclude the influence of the transient response. Consequently, the evolution of the wheel/rail contact parameters (including the contact point position, size of contact patch, normal forces, and creepages) of the left 10 wheel revolutions is obtained as the input for the wear model. Then, the wear depth corresponding to the 10 revolutions is determined by the Archard wear model and scaled by a large factor (20,852) associated with a long travel distance (550 km). As the last step of each iteration, the scaled wear depth is added around the wheel circumference to update the wheel polygonal wear according to the angle of wheel rotation. Based on the updated wheel polygonalization, a new dynamic simulation is performed and the polygonal wear is calculated once again. In order to simulate more realistic operating conditions, the running direction of the vehicle changes after every two adjacent iterations, and the wheels rotate at a random angle before each vehicle/track dynamic simulation to avoid the wheels rolling across the same part of track every time. By repeating the long-term polygonal wear iteration, the growth of wheel polygonal wear is expected to be reproduced.

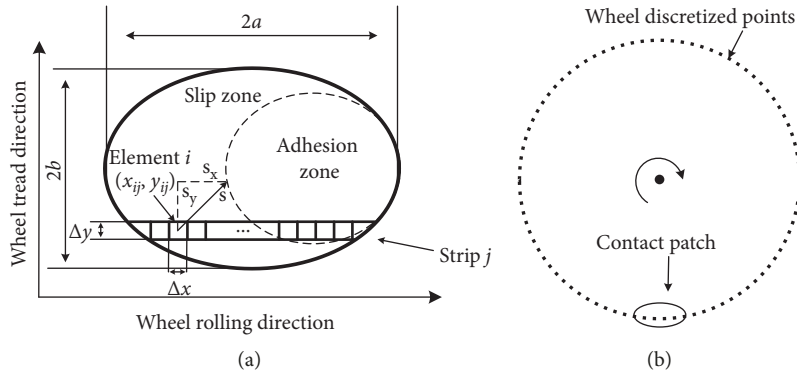


FIGURE 11: Wheel wear estimation: (a) discretization of the contact patch; (b) wear on wheel circumference.

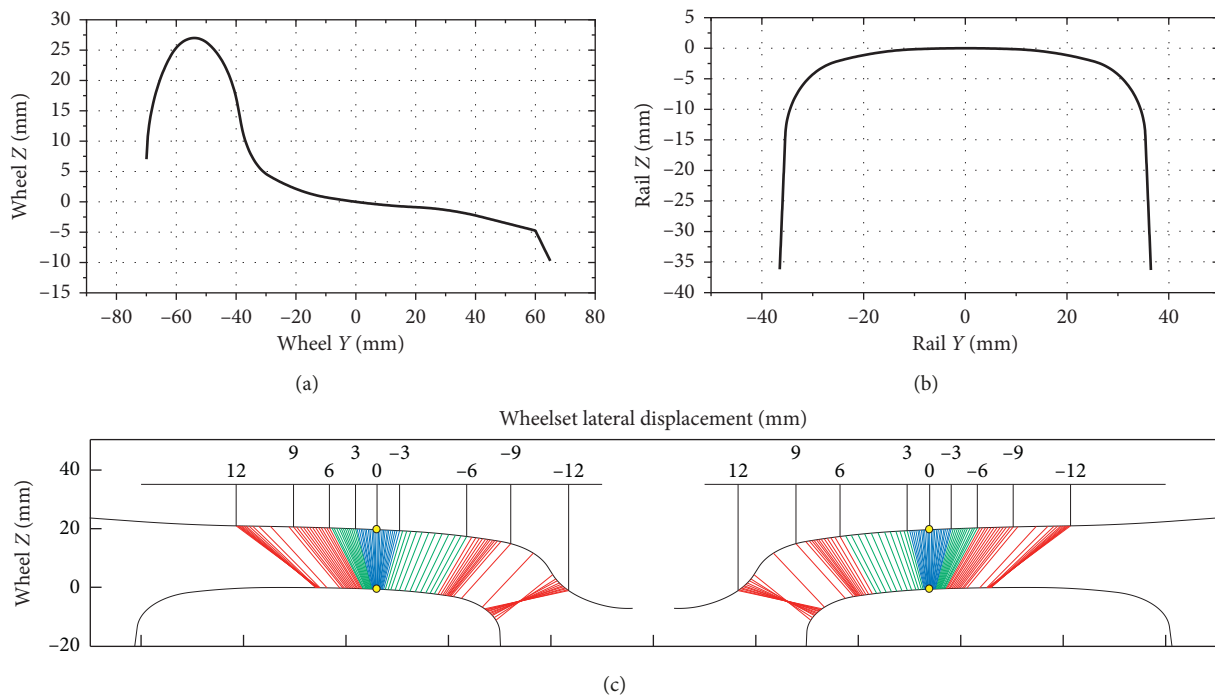


FIGURE 12: Wheel-rail contact geometry: (a) LM wheel tread profile; (b) CHN60 rail profile; (c) wheel/rail contact points distribution.

4. Results and Discussion

4.1. Verification of the Coupled Vehicle/Track Dynamic Model.
 Prior to the prediction of wheel polygonal wear, the coupled vehicle/track dynamic model is first validated by comparing the dynamic response to the measured one. The vertical accelerations of the axlebox measured immediately after wheel reprofiling with the vehicle running on the concrete bed track with DTV12 fasteners at a speed of 60 km/h and 75 km/h are used for validation. The discrete Fourier transforms of the measured data are illustrated in Figure 14: a peak is observed at approximately 50~70 Hz regardless of the speed, similarly to the STFT results in Figure 5. Moreover, other speed-independent peaks are observed at 400~450 Hz and 700~750 Hz, which contributes significantly to the axlebox vertical accelerations at

relatively high frequency. Using the wheel irregularities measured just after wheel reprofiling (cf. Figure 4) and the rail irregularity measured from the test line, simulations are performed at 60 km/h and 75 km/h. The simulation results and measured data show a good fit. According to previous studies [40], the peaks at approximately 50~70 Hz are believed to be caused by the P2 resonance, the P2 resonance is also called the vehicle/track-coupled resonance, in which the wheelset and the track vibrates in phase on the support stiffness. This resonance frequency is dominated on the vertical acceleration of the axlebox. This may be the root cause of wheel polygonalization during operation. Furthermore, the latter peaks at 400~450 Hz and 700~750 Hz could be attributed to rail bending resonance with the boundaries constrained by two wheelsets in a bogie, which corresponds to the two and three half wavelengths reflected

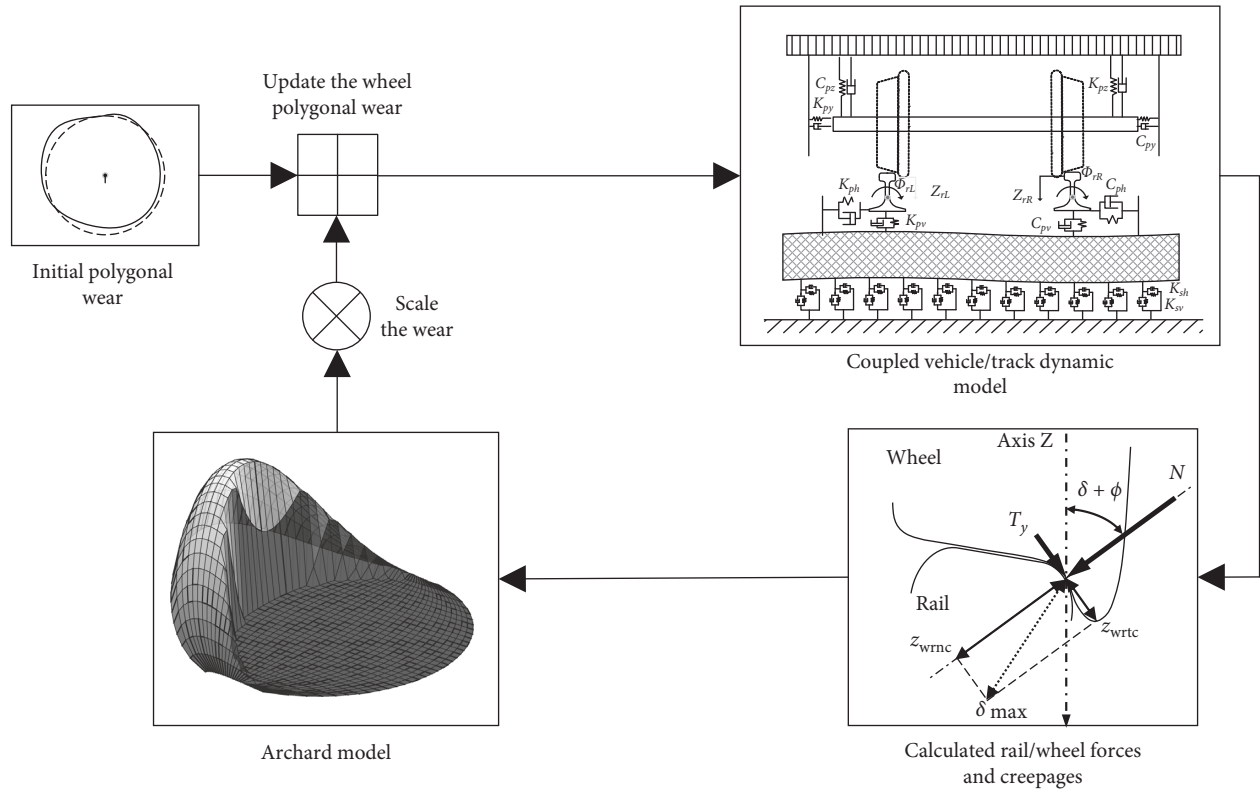


FIGURE 13: Flow chart of long-term wheel polygonalization wear iteration.

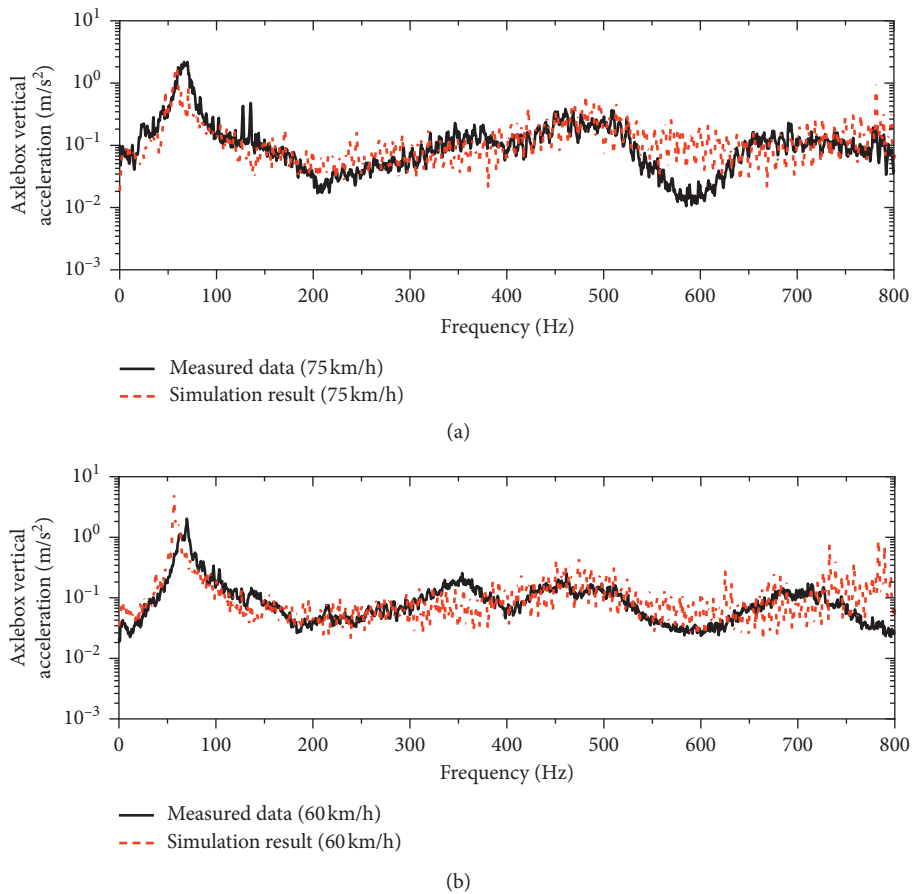


FIGURE 14: Comparison of the frequency spectra of axlebox vertical accelerations between simulations and measurements.

in the bogie wheelbase region, respectively. Such local rail bending modes are considered to contribute to the formation of rail corrugation [41].

4.2. Evolution of Wheel Polygonalization. Using the long-term wear iteration model, the development of wheel polygonalization is predicted from the measured initial wheel irregularity (Figure 4) and the vehicle speed is assumed constant at 75 km/h. Figure 15 plots the development of the radius deviation and the corresponding harmonic-order levels of the leading and trailing wheels for a bogie in 40 iteration steps (a total travel distance of 22,000 km). It is observed from Figure 15 that the 7th order harmonics has the highest increase between the initial and final polygonal wear. The roughness of the 7th order polygonalization for the leading wheel increases from -21.5 dB to 22.6 dB during the 40 iteration steps. The maximum roughness level for the trailing wheel is also the 7th order, which increases from -4.9 dB to 21.4 dB. Similar results are observed on other wheels and are not listed here. In comparison, the properties of polygonalization determined by the simulation agree with those measured before reprofiling in the field test.

Furthermore, Figure 16 illustrates the wheel/rail normal force evolution of the leading wheel with increasing iteration steps. The evolution of polygonal wear is approximately illustrated in Figures 15 and 16. In the early stage, the P2 resonance arises from the large amplitude of wheel/rail normal forces at approximately 50–70 Hz. Periodic fluctuation of the wheel/rail force then leads to periodic non-uniform wear around the wheel circumference. As a result, preliminary 7th order wheel polygonalization forms. With an increase of operating mileage, the 7th order wheel polygonalization gradually develops and in turn excites the P2 resonance. The resonance then further accelerates polygonalization wear, which indicates enhanced interaction between polygonal wear and the wheel/rail system. It is thus deduced that metro wheel polygonalization during operation originates from the P2 resonance.

4.3. Parametric Studies

4.3.1. Wheelset Flexibility. Under the large wheel/rail forces, the flexible modes of wheelset are more easily excited. And the flexibility of wheelset, especially the lower torsional and bending mode, would in turn affect the wheel/rail contact forces and creepages and may promote the formation of the polygonal wear [11, 13, 27, 29]. In order to eliminate the possibility of polygonal wear caused by wheelset flexibility, the modes of the wheelset are calculated by the finite-element method, the wheelset is formulated as hexahedron solid elements with the total number of 191,078, and the boundary of the wheelset is assumed to be free, as shown in Figure 17. The first four-order natural frequencies and generalized modal shapes of wheelset are obtained in the ANSYS software and listed in Table 2. The frequencies of first torsional mode and first bending mode are 75 Hz and

92 Hz, which are not in the range of the excitation frequency of the polygonal wear (50–70 Hz). Thus, the flexibility of the wheelset is not the root cause for the polygonal wear that we focused.

In order to get insights into the effect of wheelset flexibility on the formation of polygonal wear, the wheelset flexibility is also integrated into the vehicle dynamic model. The difficulty for modeling a flexible wheelset is its associated rotation effect. The most widely employed Lagrangian approach is not appropriate any more as the coordinates rotate with the wheelset. While in the Eulerian approach, the coordinate is not associated with the particle of the solid, which provides convenience to formulate the motion equation rotating flexible wheelset. The transformation between the Lagrangian coordinate system and Eulerian coordinate system is the crucial step. Baeza [42] presented a detailed discuss in transforming the motion equation of rotating flexible wheelset from the Lagrangian coordinate system to the Eulerian system, in which the final form of the motion equation in the Eulerian system can be expressed as

$$\ddot{q}_w + (D_w - 2\Omega\tilde{G})\dot{q}_w + (K_w + \Omega^2\tilde{C})q_w = P - \Omega^2\tilde{L}, \quad (15)$$

where q_w denotes the generalized modal coordinated of the wheelset, Ω is the angular velocity of wheel rotation, D_w and K_w represent normal coordinate generalized damping and stiffness, \tilde{G} relates to the gyroscopic effect, \tilde{C} and \tilde{L} are associated with the centrifugal effect caused by rotation, and P stands for the generalized external forces. One advantage of this approach is that the corresponding matrixes could be calculated before the real-time simulation, which can effectively reduce the computation time.

Figure 18 illustrates the vertical receptance of the wheelset with and without the wheelset rotation effect, the excitation is applied at the nominal contact point, and the measurement is at the same point. The result indicates that the rotation effect can split those modes into backward and forward modes (only bending modes) [42].

When the elastic deformation of wheelset occurs, the conventional wheel/rail trace method for contact point search is no longer applicable. On account of this, Zhong [43] developed a new “online searching contact method” in which the spatial contact position of the left and right wheel is determined individually in the dummy wheelset coordinate. This technique is employed in the present study. Then, a random white noise rail roughness is applied on a tangent track in the dynamic model, and the wheel/rail normal forces and lateral creepage response with and without wheelset flexibility are compared in Figure 19. The normal forces have not much difference between these two models. However, the lateral creepage shows a peak at round 90 Hz when using the flexible wheelset model, which is related to the first bending mode (the axle bending induces the antiphase vibration of left and right wheel disc and causes the lateral slips between wheel and rail). Furthermore, the predicted polygonal wear is compared when using the flexible wheelset and rigid wheelset, the wear depth deviation after 25 iteration steps are plotted in Figure 20, and the result

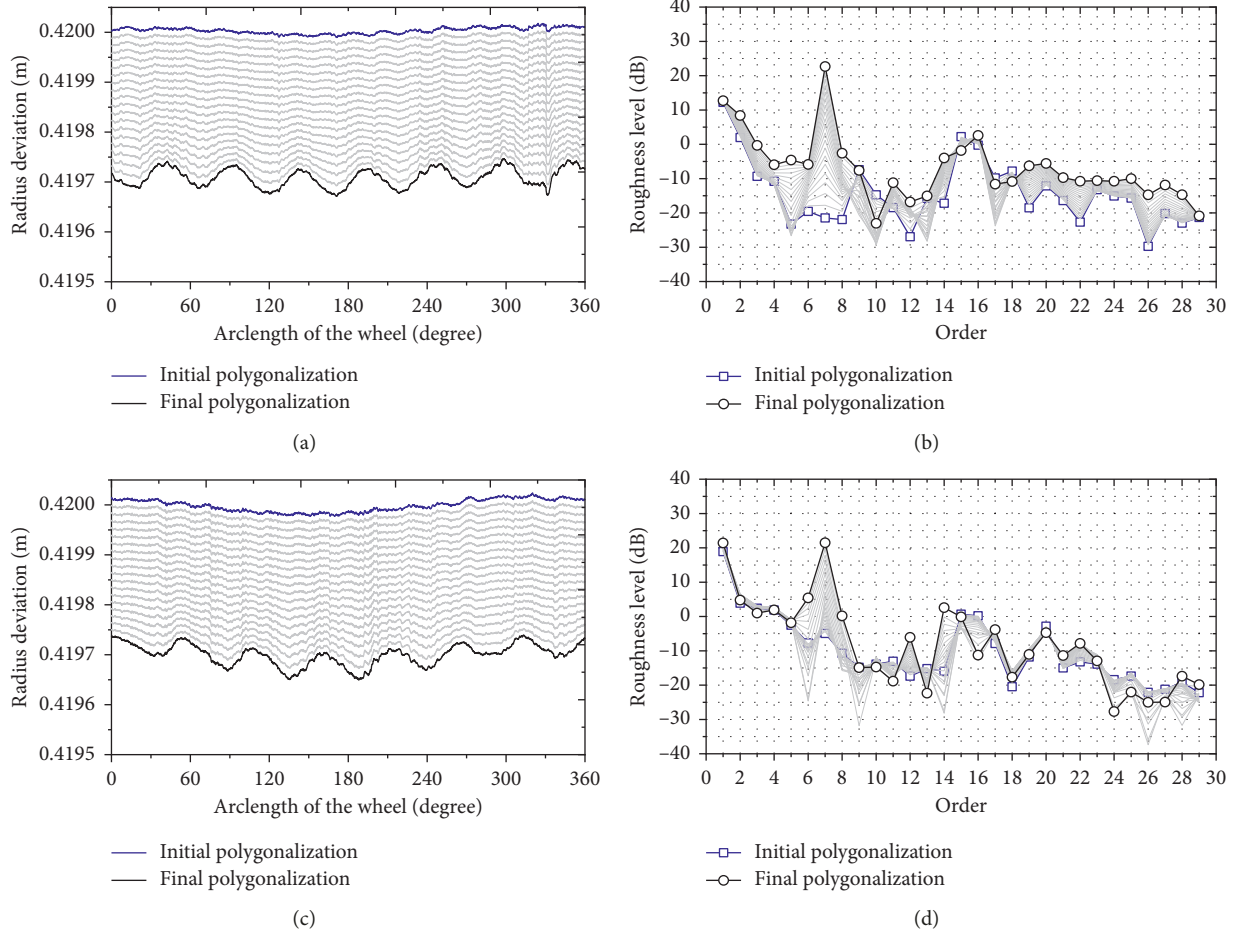


FIGURE 15: Evolution of wheel polygonalization based on the initial measured wheel irregularity, development of radius deviation, and harmonic-order levels (for a vehicle running at a speed of 75 km/h for 22,000 km): (a, b) leading wheel; (c, d) trailing wheel.

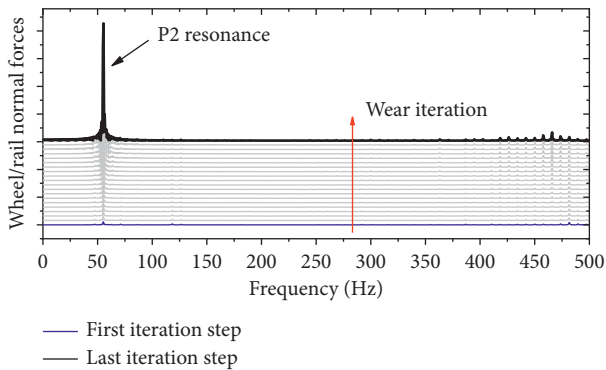


FIGURE 16: Frequency spectra of wheel/rail normal forces with increasing iteration step.

shows that the dominating order of the polygonal wear would not change when considering wheelset flexibility. However, the wheelset flexible vibration would accelerate the formation of P2 resonance-induced polygonal wear, and this is because the flexible mode leads to the larger wheel/rail creepage [27, 35].

4.3.2. Vehicle Speeds. In order to better understand the physical polygonal wear mechanism, different parameters



FIGURE 17: Wheelset finite-element model.

are considered in the polygonalization prediction. Figure 21 shows the growth of polygonal wear at vehicle speeds of 30–90 km/h. The dominant orders of polygonalization are 17th, 11th, 7th, and 6th at speeds of 30 km/h, 50 km/h, 75 km/h, and 90 km/h, respectively. However, their passing frequencies $f_{oor} = N * V / \pi D$ are 53 Hz, 57 Hz, 55 Hz, and 56 Hz, which are very close. It means that the P2 resonance-caused polygonal wear serves as the so-called “frequency-constant” mechanism [30]. As the P2 resonance frequency does not change with speed, it is unsurprising that the dominant order of polygonal wear shifts to lower orders with an increase of speed.

TABLE 2: Modes of wheelset.

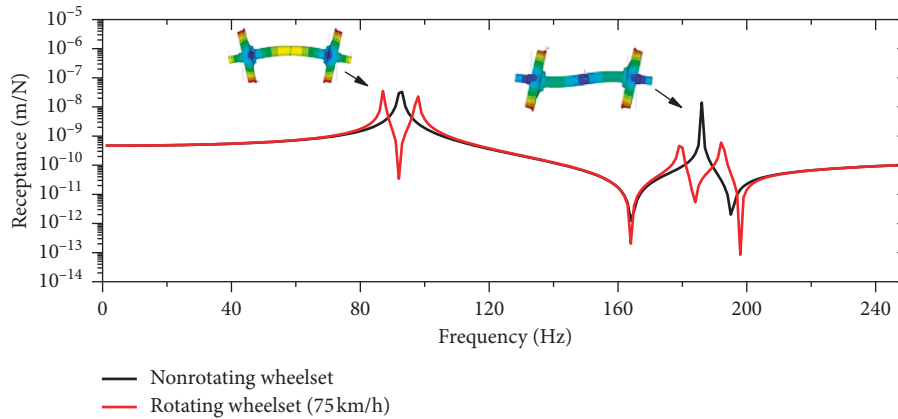
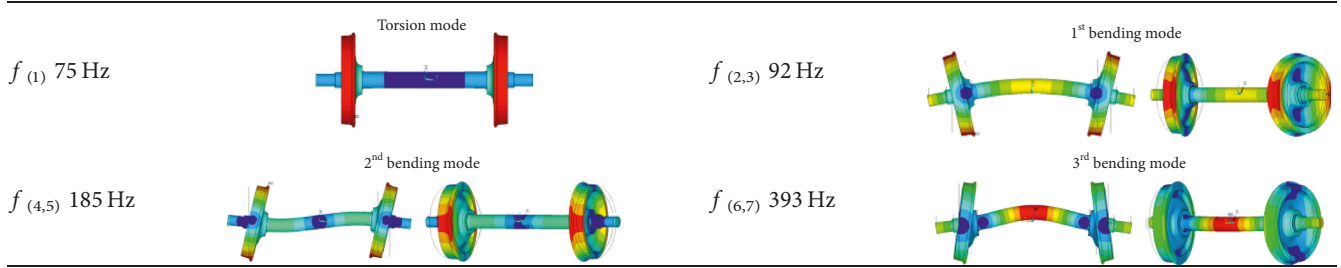


FIGURE 18: Vertical receptance at the nominal contact point of the flexible wheelset when the velocity of the wheelset is 0 and 75 km/h.

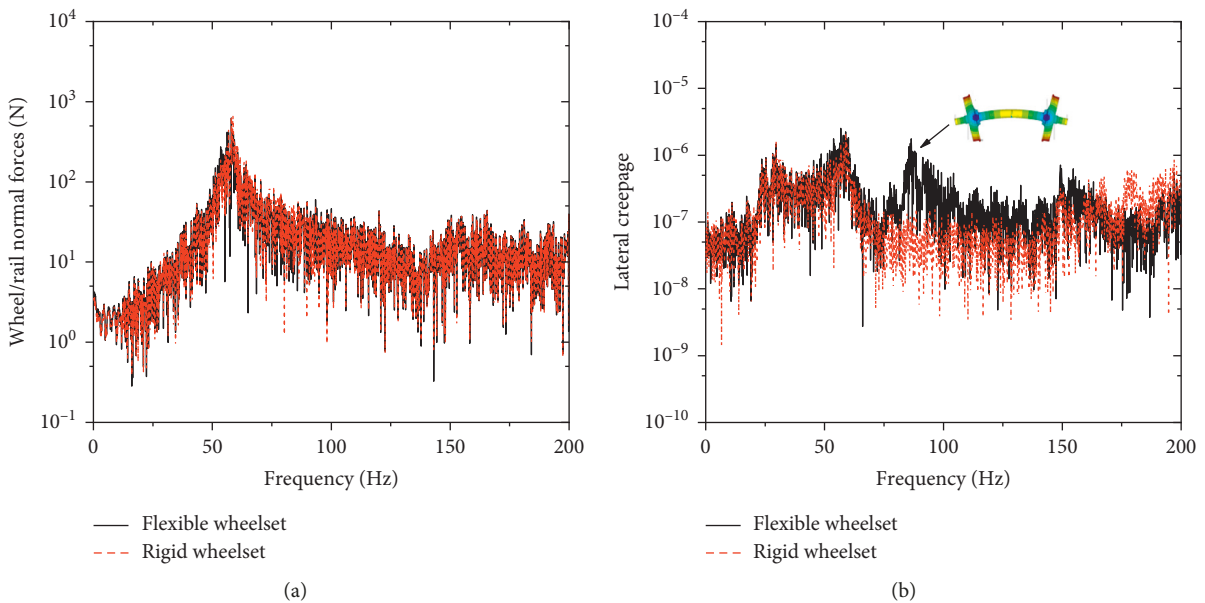


FIGURE 19: Comparison of the wheel/rail normal forces and creepage with and without wheelset flexibility.

4.3.3. *Rail Pad Stiffness.* The P2 resonance frequency largely depends on the rail pad stiffness; the greater the rail pad stiffness, the higher the P2 resonance frequency. Figure 22 illustrates the results of polygonal wear prediction for a rail pad stiffness of 35 MN/m (after 27,500 km), 55 MN/m (after

22,000 km), 75 MN/m (after 11,000 km), and 110 MN/m (after 8250 km). As expected, the dominant harmonic order changes from the 6th order to 9th order with an increase of rail pad stiffness, which correlates with the variation of P2 resonance frequency. Moreover, the larger rail pad stiffness

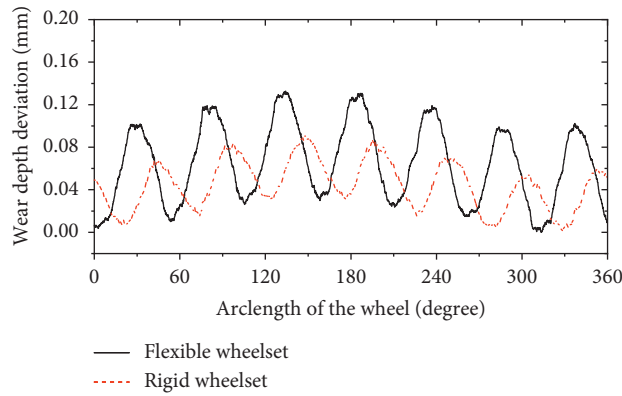


FIGURE 20: Simulated wear depth deviation after 25 iteration steps (13,750 km) with and without wheelset flexibility (75 km/h).

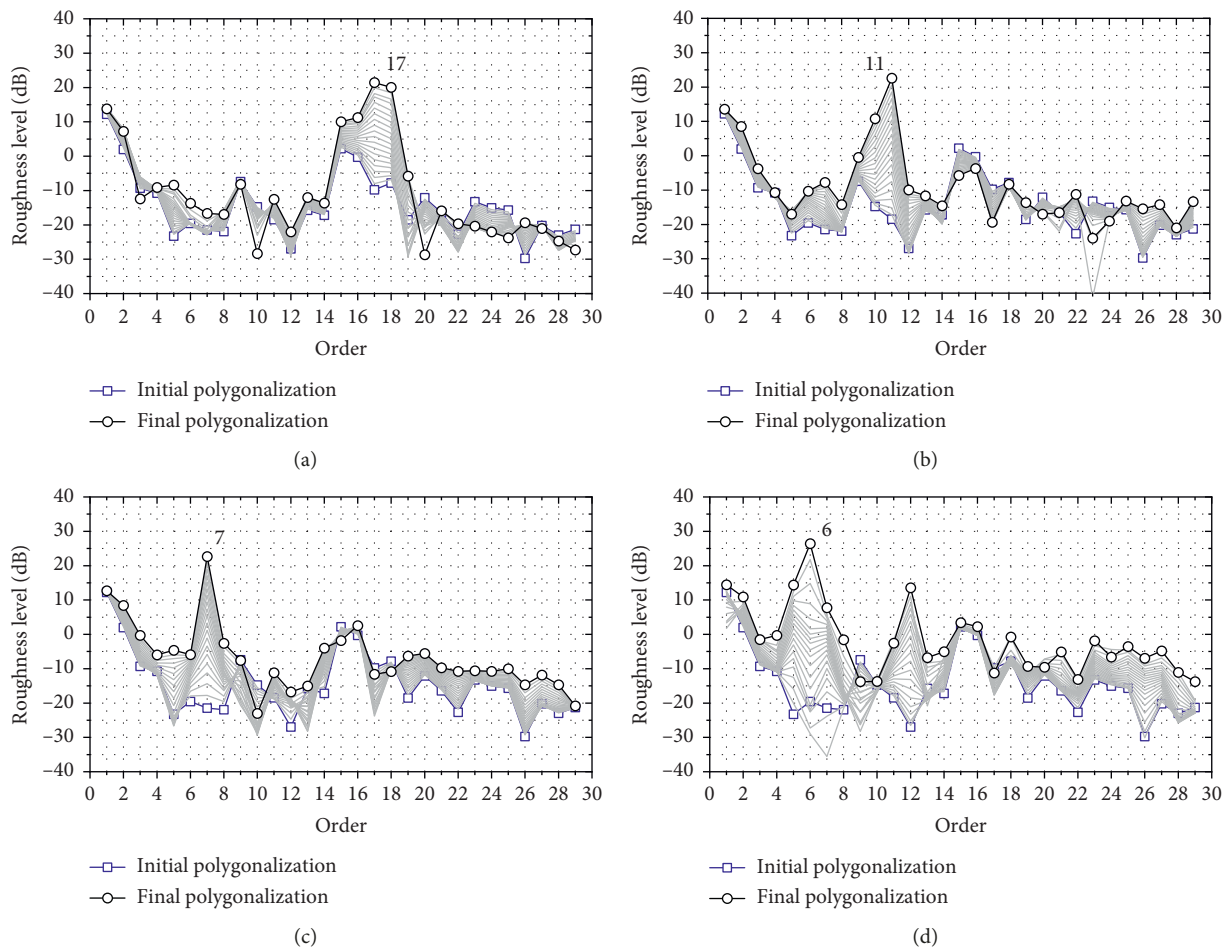


FIGURE 21: Evolution of wheel polygonalization at different vehicle speeds (after 22,000 km): (a) 30 km/h; (b) 50 km/h; (c) 75 km/h; (d) 90 km/h.

tends to accelerate the development of polygonal wear, and it is partly because that the amplitude of wheel/rail forces is induced by the P2 resonance increases with the rail pad stiffness. On the contrary, the polygonal wear would be easily generated when the perimeter of the wheel is divided evenly by the wavelength corresponding to the P2 resonance frequency. Therefore, in the simulation cases satisfying the

divisibility condition, the polygonal wear will develop very rapidly.

5. Conclusions

Train wheel polygonal wear is a significant concern in railway engineering, and the mechanism behind it remains elusive. In

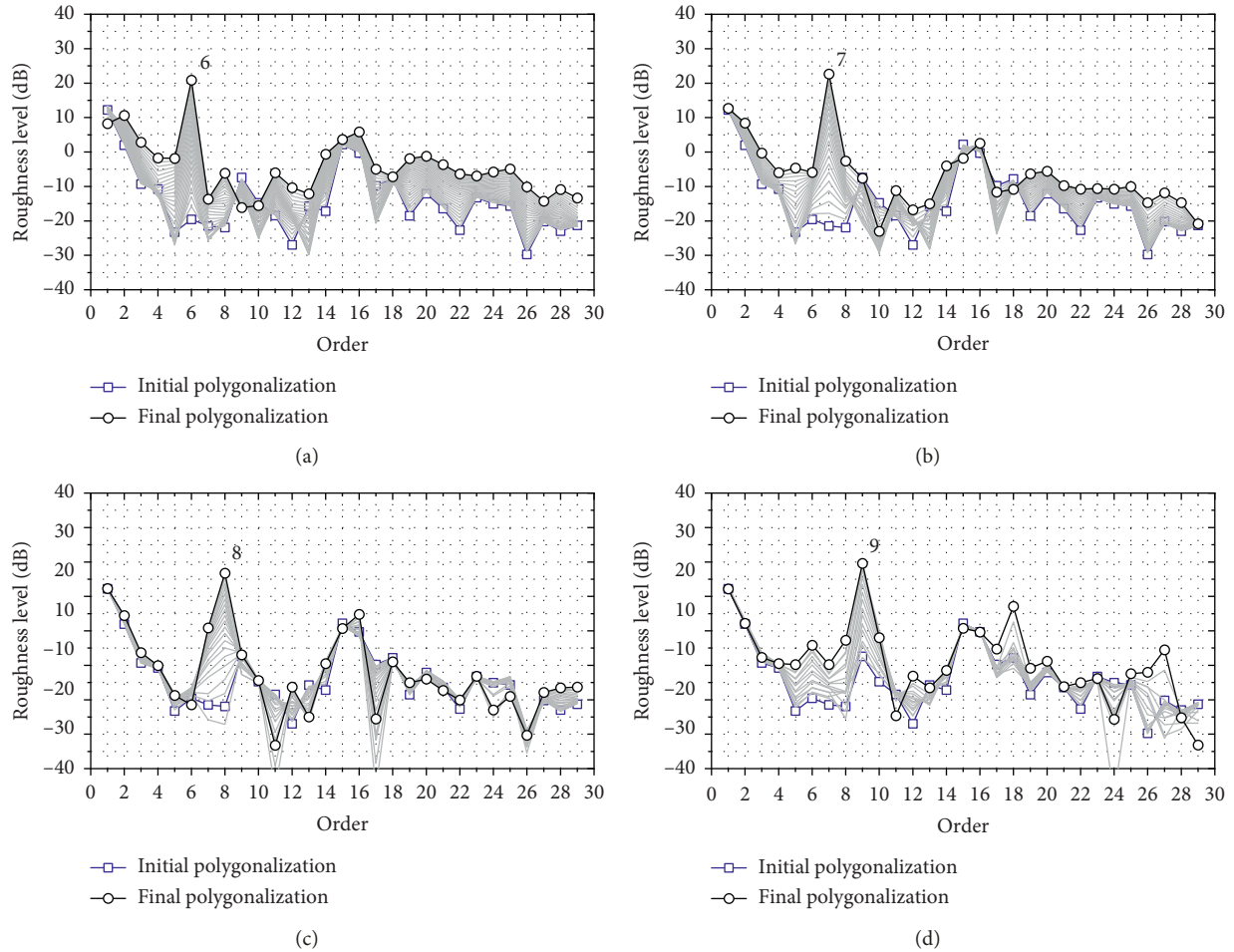


FIGURE 22: Evolution of wheel polygonalization at different rail pad stiffness values: (a) 35 MN/m after 27,500 km; (b) 55 MN/m after 22,000 km; (c) 75 MN/m after 11,000 km; (d) 110 MN/m after 8250 km.

this study, 6–8th order wheel polygonal wear was commonly measured on the trains of a specific metro line in China. A dynamic vibration test immediately after wheel reprofiling indicated that a natural resonance exists in the frequency range of 50–70 Hz, which coincides with the passing frequency of polygonal wear. In order to identify the origin of polygonal wear, we established a long-term polygonal wear iteration model consisting of a coupled vehicle/track dynamic model and Archard wear model based on multiple timescales. The growth of wheel polygonalization was predicted based on wheel irregularity measured immediately after wheel reprofiling. The simulation results revealed that P2 resonance is the main contributor to the high amplitude wheel/rail normal forces in the 50–70 Hz frequency interval and the root cause of wheel polygonal wear on the metro trains. Additionally, the effects of different parameters on the development of polygonalization were discussed. The wheelset flexibility, especially the bending mode, would aggravate the wheel/rail lateral creepage, which can accelerate the formation of polygonal wear. An increase of vehicle operating speeds will shift the dominant order of polygonal wear to lower orders because the P2 resonance frequency is speed-independent, representing a “frequency-constant” mechanism. Conversely,

P2 resonance frequency will increase with increasing rail pad stiffness and shift the dominant order of polygonal wear to higher orders.

Data Availability

The measured wheel polygonal wear and vehicle acceleration data used to support the findings of this study are available from the corresponding author upon request.

Conflicts of Interest

The authors declare that they have no conflicts of interest.

Acknowledgments

This work was supported by the National Natural Science Foundation of High Speed Rail Joint Funds of China (U1734201), the National Key R&D Program of China (2016YFB1200501-005), the National Science Foundation for Young Scientists of China (51805450), and the Opening Project of the State Key Laboratory of Traction Power of Southwest Jiaotong University (2018TPL_T04).

References

- [1] J. C. O. Nielsen and A. Johansson, "Out-of-round railway wheels—a literature survey," *Proceedings of the Institution of Mechanical Engineers, Part F: Journal of Rail and Rapid Transit*, vol. 214, no. 2, pp. 79–91, 2000.
- [2] M. Zacher, "Unrunde Räder und oberbauteifigkeit," *ETR-Eisenbahntechnische Rundschau*, vol. 45, pp. 605–610, 1996.
- [3] G. Pallgen, "Unrunde Räder an Eisenbahnfahrzeugen: Durch ortsfeste Messanlagen können unrunde Räder an Schienenfahrzeugen detektiert werden," *Der Eisenbahningenieur*, vol. 49, pp. 56–60, 1998.
- [4] W. Rode, D. Müller, and J. Villman, "Results of DB AG investigations 'out-of-round wheels,'" in *Proceedings Corrugation Symposium—Extended Abstracts, IFV Bahntechnik*, Technische Universität Berlin, Berlin, Germany, 1997.
- [5] H. P. Kaper, "Wheel corrugation on Netherlands railways (NS): origin and effects of "polygonization" in particular," *Journal of Sound and Vibration*, vol. 120, no. 2, pp. 267–274, 1988.
- [6] P. C. Dings and M. G. Dittich, "Roughness on Dutch railway wheels and rails," *Journal of Sound and Vibration*, vol. 193, no. 1, pp. 103–112, 1996.
- [7] T. Vernersson, "Thermally induced roughness of tread braked railway wheels: Part 1: brake rig experiments," *Wear*, vol. 236, no. 1–2, pp. 96–105, 1999.
- [8] T. Vernersson, "Thermally induced roughness of tread braked railway wheels: Part 2: modelling and field measurements," *Wear*, vol. 236, no. 1–2, pp. 106–116, 1999.
- [9] A. Johansson, "Out-of-round railway wheels—assessment of wheel tread irregularities in train traffic," *Journal of Sound and Vibration*, vol. 293, no. 3–5, pp. 795–806, 2006.
- [10] T. Snyder, D. H. Stone, and J. Kristan, "Wheel flat and out-of-round formation and growth, Rail Conference," in *Proceedings of the 2003 IEEE/ASME Joint*, pp. 143–148, Chicago, IL, USA, April 2003.
- [11] X. Jin, L. Wu, J. Fang, S. Zhong, and L. Ling, "An investigation into the mechanism of the polygonal wear of metro train wheels and its effect on the dynamic behaviour of a wheel/rail system," *Vehicle System Dynamics*, vol. 50, no. 12, pp. 1817–1834, 2012.
- [12] G. Tao, L. Wang, Z. Wen, Q. Guan, and X. Jin, "Measurement and assessment of out-of-round electric locomotive wheels," *Proceedings of the Institution of Mechanical Engineers, Part F: Journal of Rail and Rapid Transit*, vol. 232, no. 1, pp. 275–287, 2018.
- [13] G. Tao, L. Wang, Z. Wen, Q. Guan, and X. Jin, "Experimental investigation into the mechanism of the polygonal wear of electric locomotive wheels," *Vehicle System Dynamics*, vol. 56, no. 6, pp. 883–899, 2017.
- [14] X. Wu, M. Chi, and P. Wu, "Influence of polygonal wear of railway wheels on the wheel set axle stress," *Vehicle System Dynamics*, vol. 53, no. 11, pp. 1535–1554, 2015.
- [15] X. Wu, M. Chi, and H. Gao, "Damage tolerances of a railway axle in the presence of wheel polygonalizations," *Engineering Failure Analysis*, vol. 66, pp. 44–59, 2016.
- [16] X. Wu, S. Rakheja, S. Qu, P. Wu, J. Zeng, and A. K. W. Ahmed, "Dynamic responses of a high-speed railway car due to wheel polygonalisation," *Vehicle System Dynamics*, vol. 56, no. 12, pp. 1817–1837, 2018.
- [17] H. Shi, J. Wang, P. Wu, C. Song, and W. Teng, "Field measurements of the evolution of wheel wear and vehicle dynamics for high-speed trains," *Vehicle System Dynamics*, vol. 56, no. 8, pp. 1187–1206, 2018.
- [18] J. Zhang, G. Han, X. Xiao, R. Wang, Y. Zhao, and X. Jin, "Influence of wheel polygonal wear on interior noise of high-speed trains," *Journal of Zhejiang University-Science A*, vol. 15, pp. 1002–1018, 2014.
- [19] Y. Wu, X. Du, H.-J. Zhang, Z.-F. Wen, and X.-S. Jin, "Experimental analysis of the mechanism of high-order polygonal wear of wheels of a high-speed train," *Journal of Zhejiang University-Science A*, vol. 18, no. 8, pp. 579–592, 2017.
- [20] X. Liu and W. Zhai, "Analysis of vertical dynamic wheel/rail interaction caused by polygonal wheels on high-speed trains," *Wear*, vol. 314, no. 1–2, pp. 282–290, 2014.
- [21] L. Li, X.-B. Xiao, and X.-S. Jin, "Interaction of subway LIM vehicle with ballasted track in polygonal wheel wear development," *Acta Mechanica Sinica*, vol. 27, no. 2, pp. 297–307, 2011.
- [22] T. Mazilu, M. Dumitriu, C. Tudorache, and M. Sebeşan, "Wheel/rail interaction due to the polygonal wheel," *UPB Scientific Bulletin*, vol. 73, 2011.
- [23] J. Han, S. Zhong, X. Xiao, Z. Wen, G. Zhao, and X. Jin, "High-speed wheel/rail contact determining method with rotating flexible wheelset and validation under wheel polygon excitation," *Vehicle System Dynamics*, pp. 1–17, 2017.
- [24] J. Wang, C. Song, P. Wu, and H. Dai, "Wheel reprofiling interval optimization based on dynamic behavior evolution for high speed trains," *Wear*, vol. 366–367, pp. 316–324, 2016.
- [25] A. Johansson and C. Andersson, "Out-of-round railway wheels—a study of wheel polygonalization through simulation of three-dimensional wheel-rail interaction and wear," *Vehicle System Dynamics*, vol. 43, no. 8, pp. 539–559, 2005.
- [26] K. Popp and W. Schiehlen, *System Dynamics and Long-Term Behaviour of Railway Vehicles, Track and Subgrade*, Springer Science & Business Media, Berlin, Germany, 2003.
- [27] B. Morys, "Enlargement of out-of-round wheel profiles on high speed trains," *Journal of Sound and Vibration*, vol. 227, no. 5, pp. 965–978, 1999.
- [28] P. Meinke and S. Meinke, "Polygonalization of wheel treads caused by static and dynamic imbalances," *Journal of Sound and Vibration*, vol. 227, no. 5, pp. 979–986, 1999.
- [29] M. Meywerk, "Polygonalization of railway wheels," *Archive of Applied Mechanics (Ingenieur Archiv)*, vol. 69, no. 2, pp. 105–120, 1999.
- [30] A. Johansson, *Out-of-Round Railway Wheels—Causes and Consequences An Investigation Including Field Tests, Out-of-Roundness Measurements and Numerical Simulations*, Chalmers University of Technology, Göteborg, Sweden, 2005.
- [31] W. Zhang, Z. Shen, and J. Zeng, "Study on dynamics of coupled systems in high-speed trains," *Vehicle System Dynamics*, vol. 51, no. 7, pp. 966–1016, 2013.
- [32] X. Xiao, L. Ling, and X. Jin, "A study of the derailment mechanism of a high speed train due to an earthquake," *Vehicle System Dynamics*, vol. 50, no. 3, pp. 449–470, 2012.
- [33] V. Garg, *Dynamics of Railway Vehicle Systems*, Academic Press, Cambridge, MA, USA, 1984.
- [34] I. Zobory, "Prediction of wheel/rail profile wear," *Vehicle System Dynamics*, vol. 28, no. 2–3, pp. 221–259, 1997.
- [35] X. Wu, S. Rakheja, W. Cai, M. Chi, A. K. W. Ahmed, and S. Qu, "A study of formation of high order wheel polygonalization," *Wear*, vol. 424–425, pp. 1–14, 2019.
- [36] J. C. O. Nielsen, R. Lundén, A. Johansson, and T. Vernersson, "Train-track interaction and mechanisms of irregular wear on wheel and rail surfaces," *Vehicle System Dynamics*, vol. 40, no. 1–3, pp. 3–54, 2003.
- [37] K. Knothe and A. Groß-Thebing, "Short wavelength rail corrugation and non-steady-state contact mechanics," *Vehicle System Dynamics*, vol. 46, no. 1–2, pp. 49–66, 2008.

- [38] T. Jendel, "Prediction of wheel profile wear-comparisons with field measurements," *Wear*, vol. 253, no. 1-2, pp. 89-99, 2002.
- [39] M. Arnold and H. Netter, "Approximation of contact geometry in the dynamical simulation of wheel-rail," *Mathematical and Computer Modelling of Dynamical Systems*, vol. 4, no. 2, pp. 162-184, 1998.
- [40] J. C. O. Nielsen, "High-frequency vertical wheel-rail contact forces-Validation of a prediction model by field testing," *Wear*, vol. 265, no. 9-10, pp. 1465-1471, 2008.
- [41] A. Johansson and J. C. O. Nielsen, "Rail corrugation growth-Influence of powered wheelsets with wheel tread irregularities," *Wear*, vol. 262, no. 11-12, pp. 1296-1307, 2007.
- [42] L. Baeza, J. Fayos, A. Roda, and R. Insa, "High frequency railway vehicle-track dynamics through flexible rotating wheelsets," *Vehicle System Dynamics*, vol. 46, no. 7, pp. 647-659, 2008.
- [43] S. Zhong, X. Xiao, Z. Wen, and X. Jin, "Effect of wheelset flexibility on wheel-rail contact behavior and a specific coupling of wheel-rail contact to flexible wheelset," *Acta Mechanica Sinica*, vol. 32, no. 2, pp. 252-264, 2015.

